PAPER • OPEN ACCESS

Fabrication of human myocardium using multidimensional modelling of engineered tissues

View the article online for updates and enhancements.

PAPER

Fabrication of human myocardium using multidimensional modelling of engineered tissues

Pilar Montero-Calle[1,13], María Flandes-Iparraguirre[1,13], Konstantinos Mountris[2,3], Ana S de la Nava[4,12], Nicolás Laita[2], Ricardo M Rosales[2,7], Olalla Iglesias-García[1], Elena M de-Juan-Pardo[5] ⓘ, Felipe Atienza[4,6,12] ⓘ, María Eugenia Fernández-Santos[4,12] ⓘ, Estefanía Peña[2,7], Manuel Doblaré[2,7] ⓘ, Juan J Gavira[8,9], Francisco Fernández-Avilés[4,6,12] ⓘ, Felipe Prósper[1,9,10,11], Esther Pueyo[2,7] and Manuel M Mazo[1,9,10,*] ⓘ

1 Regenerative Medicine Program, Cima Universidad de Navarra, Pamplona, Spain
2 Aragón Institute for Engineering Research (I3A) University of Zaragoza, Zaragoza, Spain
3 Department of Mechanical Engineering, University College London, London, United Kingdom
4 Hospital General Universitario Gregorio Marañón, Instituto de Investigación Sanitaria Gregorio Marañón, Madrid, Spain & CIBERCV, ISCIII, Madrid, Spain
5 T3mPLATE, Harry Perkins Institute of Medical Research, QEII Medical Centre and UWA Centre for Medical Research, The University of Western Australia, Perth, Australia
6 Universidad Complutense, Madrid, Spain
7 CIBER de Bioingeniería, Biomateriales y Nanomedicina (CIBER-BBN), Zaragoza, Spain
8 Department of Cardiology, Clínica Universidad de Navarra, Pamplona, Spain
9 Instituto de Investigación Sanitaria de Navarra (IdiSNA), Pamplona, Spain
10 Hematology and Cell Therapy, Clínica Universidad de Navarra, Pamplona, Spain
11 CIBER de Cáncer (CIBERONC, team CB16/12/00489), Pamplona, Spain
12 Centro de Investigación Biomédica en Red de Enfermedades Cardiovasculares (CIBER-CV), Madrid, Spain
13 Equal contribution
* Author to whom any correspondence should be addressed.

E-mail: mmazoveg@unav.es

Abstract

Biofabrication of human tissues has seen a meteoric growth triggered by recent technical advancements such as human induced pluripotent stem cells (hiPSCs) and additive manufacturing. However, generation of cardiac tissue is still hampered by lack of adequate mechanical properties and crucially by the often unpredictable post-fabrication evolution of biological components. In this study we employ melt electrowriting (MEW) and hiPSC-derived cardiac cells to generate fibre-reinforced human cardiac minitissues. These are thoroughly characterized in order to build computational models and simulations able to predict their post-fabrication evolution. Our results show that MEW-based human minitissues display advanced maturation 28 post-generation, with a significant increase in the expression of cardiac genes such as MYL2, GJA5, SCN5A and the MYH7/MYH6 and MYL2/MYL7 ratios. Human iPSC-cardiomyocytes are significantly more aligned within the MEW-based 3D tissues, as compared to conventional 2D controls, and also display greater expression of C × 43. These are also correlated with a more mature functionality in the form of faster conduction velocity. We used these data to develop simulations capable of accurately reproducing the experimental performance. In-depth gauging of the structural disposition (cellular alignment) and intercellular connectivity (C × 43) allowed us to develop an improved computational model able to predict the relationship between cardiac cell alignment and functional performance. This study lays down the path for advancing in the development of *in silico* tools to predict cardiac biofabricated tissue evolution after generation, and maps the route towards more accurate and biomimetic tissue manufacture.

1. Introduction

The ability to replace failing or injured organs, as well as to generate accurate models and testing platforms, would boost our capacity to treat currently incurable pathologies, to extend our knowledge of human physiology and development, as well as to increase the accuracy of preclinical tests for new therapies and drugs. Currently, cardiovascular diseases remain the number one cause of death worldwide [1], and myocardial-related complications stand amongst the main causes of drug withdrawal, either from the development pipeline or from the market [2]. Therefore, being able to build human myocardial tissues in the laboratory is highly desirable [3].

The last 15 years have seen extraordinary developments in different areas that together bring researchers closer to achieving this objective. Firstly, human cellular reprogramming has opened the way for obtaining large numbers of human cardiac cells, be they cardiomyocytes (CMs), vascular cells or cardiac fibroblasts [4–6]. Concomitantly, material science has yielded a range of biocompatible natural, synthetic and semi-synthetic materials able to comply with the main requirements of engineering cardiac tissues (reviewed in [3]). At the same time, the revolutionary application of additive manufacturing, with its best known format being 3D bioprinting, is able to generate human engineered myocardial tissues at the micro and macroscales [7–10].

Crucially, some of the most important roadblocks have been addressed by intense research and are progressively being resolved. Cellular immaturity is a prominent feature of human pluripotent stem cell-derived cardiac cell types, including human induced pluripotent stem cells (hiPSCs) [11]. Long term culture [12], dynamic electromechanical stimuli [13, 14], or *in vivo* transplantation [15–17] have all shown remarkable effects upon the phenotype and function of hiPSC-derived cardiac tissues, although they still fall short of resembling adult human properties. Technological advances in additive manufacturing have delivered heightened printing precision [18, 19], and paved the way for the derivation of autologous biomaterials and cells [20]. However, two issues still need further attention: (a) the capacity of generated tissues to replicate and withstand the mechanical environment of the cardiac wall has still not been fully replicated, and (b) the post-fabrication evolution of the bio artificial myocardium is still in need of improvement.

Fibre reinforcement can significantly upgrade the mechanical properties of soft materials, including biocompatible hydrogels [21]. Solution electrospinning has been a classical method for obtaining fibrous substrates, but it lacks accurate control over 3D deposition and depends on toxic solvents. Melt electrowriting (MEW) has the capacity to generate fibres of the order of magnitude of the size of a human cell, with extremely precise 3D positioning [22, 23]. MEW

fibres have the potential to reinforce most soft materials employed in cardiac tissue engineering, providing not only better material properties, but also alignment cues for CMs, which is crucial for the optimal development of a bio artificial human myocardium, as recently demonstrated [24].

As an additive manufacturing technology, MEW can benefit from CAD/CAM strategies for the fabrication of highly biomimetic bioengineered tissues, as has been shown for cardiac 3D bioprinting [25]. However, the biofabricated tissue will evolve beyond the initial design. This can be due to the presence of living or biological components, such as natural extracellular matrix (ECM) molecules, cytokines or cells [26]. Also, the application of mechanical or electrical stimuli will cause it to remodel, both structurally and functionally [14, 27]. Finally, *in vivo* transplantation will induce pronounced changes on these parameters, arising from factors such as the ingrowth (or its absence) of vascularization, presence of inflammation, fibrotic encapsulation or, for cardiac tissue, electromechanical coupling to the endogenous myocardium [28]. This has fundamental implications for the fabrication of biotissues, as regardless of the accuracy of the engineered replicate at the moment of assembly, their post-fabrication evolution can result in a final product with characteristics that diverge greatly from those initially designed.

However, assessment of all the individual variables affecting each fabricated tissue development would require an enormous amount of time and resources. New predictive tools grounded on biological and mechanical information would greatly streamline this process. One such tool is *in silico* modelling and simulation, which has become a powerful asset to accurately represent and predict cardiac electro-mechanical behaviour from sub-cellular to whole-organ scales. We propose using *in silico* tools to tackle this post-fabrication problem. In this manner, the gap between what is fabricated and what the tissue actually becomes could be predicted *in antecessum*, ensuring the resulting product follows the required specifications at both structural and functional levels.

In the present study, we take the first step towards the development of advanced computational models for the optimized fabrication of human cardiac tissue. As a starting point, we employ a simple MEW-design to fabricate a fibre reinforcement of a biological hydrogel in medical-grade poly-ε-caprolactone (mPCL). Human CMs are produced from hiPSCs and incorporated to the system, generating cardiac minitissues. We perform a detailed characterization of these tissues, at structural and functional levels, and employ this information to adjust the newly developed *in silico* models. Our results show that the isometric MEW-reinforcement results in enhanced hiPSC-CM gene expression, alignment and, importantly, advanced functionality. We analyse in detail the organization of hiPSC-CMs within tissues of varying

pore sizes, to gauge how the specific engineered niche impacts cellular alignment and inter-connectivity. Finally, the generated multidimensional information is employed to inform a novel computational model, able for the first time to perform predictions correlating the fabricated tissue structure with its functional outcome.

2. Materials and methods

All products from Thermo Fisher unless otherwise stated.

2.1. Melt electrowriting (MEW)
Fibre scaffolds were printed in mPCL (Purasorb PC 12, Corbion) using a purpose-built MEW device (QUT, Queensland, Australia, figure 1(a)). mPCL pellets were loaded on a 3 ml plastic syringe and molten at 80 °C for 2 h before being connected to a tube delivering pressurized N_2. Voltage was slowly increased until the jet was stable, and printing maintained (no coiling or whipping). We tested a range of printing conditions by varying collector speed, pressure, head and nozzle temperatures and needle diameter.

2.2. Mechanical analysis
Uniaxial tensile tests were performed on a universal testing machine (Instron Microtester 5548 system) using a 10 N load cell. Rectangular scaffold strips (30 mm × 7 mm) were tested. An optical measurement system (Instron 2663–281 video-extensometer) was used to monitor the strain. In order to analyse the anisotropy of the scaffolds, equibiaxial tests were also performed on Instron BioPuls™ low-force planar-biaxial testing system with a camera system to track the strain. Square specimens, 40 × 40 mm, were prepared. Uniaxial and equibiaxial tests were performed at a rate of 1 mm min^{-1} at room temperature until rupture of the scaffold. At least six samples for each scaffold and testing condition were tested. Mechanical parameters as elastic stress and strain (σ_{el} and ε_{el}) and tangent modulus at stress–strain elastic region (E_T) were determined from the uniaxial engineering stress–strain curves. Finally, isotropy was computed as the ratio between the engineering stress on x- and y-direction of the printing plane at 15% of strain from the equibiaxial curves (isotropy ratio (IR); IR = 1 means full isotropy).

2.3. hiPSC culture, differentiation and FACS
The human episomal iPSC line and the WTC GcAMP hiPSC line (WTC11-AAV-CAG-GCaMP6, a kind gift from Prof Bruce Conklin, Gladstone Institutes) were routinely maintained in E8 medium on growth factor reduced matrigel (GFR-MG) coated plastic surfaces (1:180 dilution), and passaged 1:15 using 0.5 mM EDTA every 4–5 d. For differentiation towards CM,

a biphasic Wnt modulation protocol [4] was used with minor modifications. Briefly, upon 80%–90% confluence, media were changed to RPMI supplemented with B27 minus insulin (RPMI B27−) and 6–8 μM CHIR99021 (Axon Medchem). About 24 h later, medium was replaced with RPMI B27− for 2 d, and then replaced with RPMI B27− and 2 μM C59 (Axon Medchem) for 48 h. After 2 d in RPMI B27−, differentiations were maintained in RPMI supplemented with full B27 (RPMI B27). Beating usually started at this point or 1–2 d later. About 48 h afterwards, cells were subjected to 2 cycles of 3 d in RPMI no glucose supplemented with 4 mM lactate. Finally, medium was refreshed with RPMI B27 before isolation, making a total of 22–25 d for the whole process.

FACS was performed to determine differentiation purity. For this, the Fix & Perm kit was employed following manufacturer's instructions, with a primary antibody against cardiac troponin T (1:100) and an Alexa Fluor 488 conjugated secondary antibody (1:200).

2.4. CM isolation and construct generation
Once differentiation was finished, hiPSC-CMs were washed three times in 0.5 mM EDTA in phosphate buffered saline (PBS) and incubated for 7–10 min in TrypE at 37 °C for monolayer dissociation. Cells were gently recovered, pooled and counted. One million hiPSC-CMs were embedded in GFR-MG (1:1) and cast on printed 0.25 mm^2 mPCL scaffolds in a silicon mould (40 μl total volume). Samples were incubated at 37 °C for 1 h before topping up with medium. Cells were also plated on slide chambers (Ibidi) as controls. hiPSC-CMs were plated in RPMI B27 supplemented with 5 μM Y27632 (Tocris) to enhance survival after dissociation. On the next day, medium was refreshed without Y27632, and every other day from there on.

2.5. Live/dead staining
Cell survival was assessed with the Live/dead kit, following manufacturer's instructions. In brief, calcein AM and ethidium homodimer were both diluted 1/500 in RPMI B27, added to samples and incubated for 45 min at 37 °C, after which media were changed and samples imaged in a Leica DMIL LED epifluorescence microscope.

2.6. RNA extraction, RT, quantitative real time-PCR
Total RNA was extracted with TRI Reagent (Sigma) following the manufacturer's instructions. RNA content and purity were determined using a Nanodrop (Qiagen). Retrotranscription was performed using the Prime Script RT Reagent (Takara) with up to 500 ng of RNA per sample as per manufacturer's instructions. Afterwards, they were further diluted to 200 μl using sterile water. Quantitative real time PCR was performed with 5 ng of cDNA and the

primers shown in table S1, in an Applied Biosystems™ PowerUp™ SYBR™ Green Master Mix in a QuantStudio 5, using fast mode as follows: 20′ at 95 °C followed by 40 cycles of 95 °C for 1′ and 20′ at the annealing temperature, plus the melting curve to confirm specificity of the reaction. GAPDH was selected as a housekeeping and results analysed using the $2^{-\Delta\Delta Ct}$ method. All samples were measured in triplicate.

2.7. Immunofluorescence, confocal microscopy and image processing

For staining, samples were washed three times in PBS, fixed in 10% buffered formalin for 30 min at RT, followed by three washes in PBS and stored at 4 °C until use. Samples were stained overnight at 4 °C with anti-cardiac α-actinin (1:200), anti-connexin-43 after 1% Tween20 permeabilization. Appropriate secondary antibodies were employed (Alexa Fluor 488- or 594-conjugated, 1:200). Images were recorded using an LSM 800 Zeiss Confocal microscope and processed using Fiji.

2.8. Z-band spacing and sarcomere directionality analysis

Alpha-actinin confocal stacks from 2D and 3D samples were used for quantifying Z-band spacing and sarcomere orientation. A custom macro was developed based on Fiji (available upon request). A minimum of 10 and maximum of 30 sarcomeres were analysed per plane, with an interplane separation of at least 20 μms. User was blinded to the group of origin to avoid any bias in the analysis.

2.9. Optical mapping

2.9.1. Calcium transient acquisition and mapping

For calcium transient (CaT) imaging, samples were stained by immersion in Tyrode's solution medium with Fura 2AM (Ca^{2+} sensitive probe, TEFLabs, Inc., Austin, TX, United States) at 10 μM for 30 min under incubation conditions (37 °C, 5% CO$_2$) [29]. Ca^{2+} transients are used as a surrogate for action potentials (APs) and to visualize propagation patterns due to the increased recorded fluorescence amplitude compared to voltage dyes. After dye incubation, culture medium was changed to Tyrode's solution at 37.0 °C (containing, in mM:NaCl 120, NaHCO$_3$ 25, H$_2$O$_4$PNa.H$_2$O 1.2, MgCl$_2$ 1, glucose 5.5, CaCl$_2$ 1.8, KCl 5.4 and albumin 0.04 g l^{-1}).

In order to excite Fura-2AM, cell cultures were illuminated with two filtered UV LED light sources (peak output 400 mW; peak wavelength 380 nm; Nichia, Tokushima, Japan), with a plano-convex lens (LA1951; focal length = 25.4 mm; Thorlabs, Newton, NJ, United States) and a UV excitation filter (FF01-380/14; Semrock) [29]. Fluorescence was recorded using an electron-multiplying charge-coupled device (EMCCD; Evolve-128: 128 × 128, 24 μm × 24 μm-square pixels, 16 bit; Photometrics,

Tucson, AZ, United States) with a custom emission filter (ET525/50-+800/200M; Chroma Technology) suitable for Fura-2AM emission placed in front of a high-speed camera lens (DO-2595; Navitar Inc., Rochester, NY, United States). Fifteen-second movies of fluorescence were recorded at 142.9 frames/s throughout the protocol duration. The area of the field of view was ∼5 mm × 5 mm (128 pixels × 128 pixels) and included the entire MEW composite.

2.9.2. Optical data processing and analysis

Custom software written in MATLAB was used to perform optical mapping image processing and analysis [30]. Data was filtered to remove fluorescence noise, applying a spatial Gaussian filter (kernel size = 5) and a temporal smoothing filter (kernel size = 5) as described in previous studies [31]. Finally, CaT signals of each pixel were normalized between 0 and 1 [32].

2.9.3. In silico *modelling and simulation*

The effect of the fibre scaffold on the electrical activation of cultured hiPSC-CMs was assessed by computational modelling and simulation using the finite element method (FEM). Isoparametric quadrilateral and hexahedral elements were used to construct mesh representations of hiPSC-CMs cultured in conventional 2D surfaces and in 3D MEW scaffolds, respectively. Cellular electrophysiology of hiPSC-CMs was represented using the Paci *et al* AP model [33]. Electrical impulse propagation was described using the monodomain model [34]. The longitudinal conductivity (i.e. in the myocardial fibre direction) was particularly set for each simulation, with a transversal-to-longitudinal conductivity ratio of 0.15 in all cases. FEM simulations were performed using the electrophysiology solver ELECTRA [35, 36].

4. Results

4.1. MEW-scaffold optimization and mechanical characterization

The fabrication of MEW-based engineered human myocardium critically relies on two components: a pre-designed polymeric scaffold and a biological filler. For the present study, mPCL was the polymer of choice, as this is the gold standard material for MEW [37], demonstrating excellent processability and reproducibility of printed designs. As main biological filler, we used hiPSC-CMs in order to gather specific information on the influence of the construct characteristics on this specific cell type. Cells were embedded in GFR-MG to provide an initial but transient 3D environment, as Matrigel would disappear within days and allow hiPSC-CM-to-CM interaction. Although mPCL demonstrates optimal fabrication properties, the resulting MEW fibres constitute

Figure 1. Set up of MEW conditions for the generation of an optimal polymeric fibre reinforcement. (a) MEW device. (b) Example of printing results. (c) Example of printing conditions tested. Selected condition is #2. (d) Measurement of fibre diameter, fibre spacing and maximum printing error for the 3 exemplified printing condition sets. (e) and (f) Confocal IF for cardiac α-actinin, showing the intimate interaction between hiPSC-CMs and the printed mPCL fibres, where 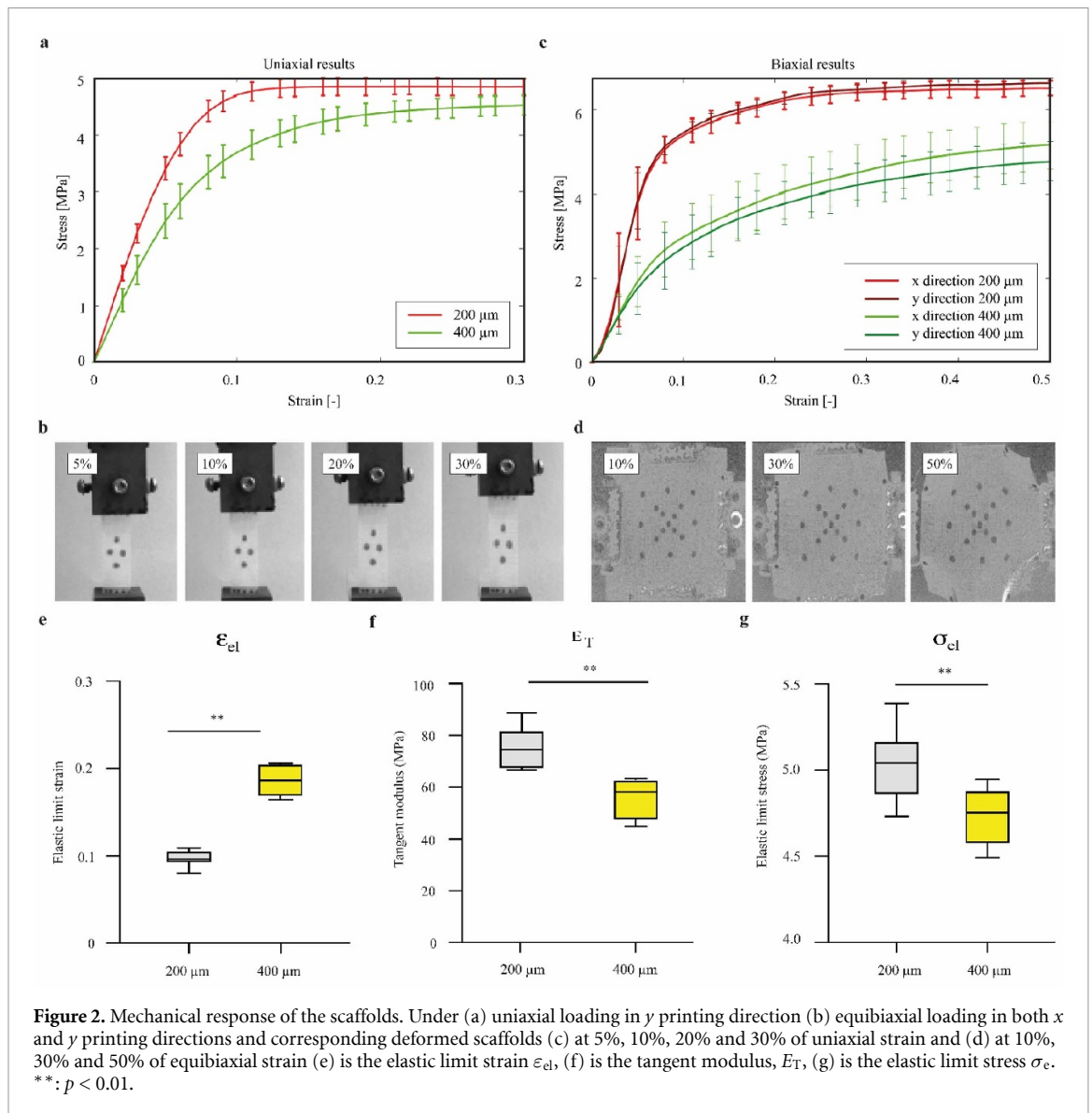cells wrap around the fibres, developing regular sarcomeric striations. Scale bars: (b): 500 μm; (e): 25 μm; (f): 20 μm.

a hyper-stiff attachment surface for cardiac cells, several orders of magnitude above the cardiac micromechanical environment [38, 39], which can lead to an isometric contraction (CM contraction without cell shortening) as usually seen on conventional plastic or glass culture surfaces. As planned, we tested a range of printing conditions (three representative examples are shown in figure 1(b) alongside their printing details in figure 1(c)). The chosen printing settings (8 kV, 7 mm nozzle-to-collector gap, 2.5 bar, 80/60 °C head/nozzle, 300 mm s^{-1} collector speed, 22 G syringe tip) produced fibres around 20 μm in diameter (figure 1(d)). To test if this fibre size allowed the attachment of few individual CMs, to minimize contact with the hyper-stiff mPCL fibres, hiPSCs were differentiated to CMs by a chemically-defined biphasic Wnt-modulation protocol, followed by a metabolic enrichment by glucose deprivation in the presence of lactate (figure S1(a)). This protocol produced beating monolayers (movie S1) of highly pure hiPSC-CMs (>90% TNNT+ by FACS, figure S1(b)), with presence of well-defined cardiac sarcomeric striations and a gene expression profile characteristic of human cardiac cells (figures S1(c) and (d)). When hiPSC-CMs were plated on the 20 μm-fibre diameter MEW scaffolds, cells were able to attach, spread and organize their sarcomeric structures (figures 1(e) and (f)). As hypothesized, confocal microscopy analysis showed that the fibres of the selected diameter were engulfed by 2–4 cells, thus decreasing the interaction of human CMs with the hyper-stiff mPCL fibres. Once we determined these fibre dimensions were able to support the fabrication of human cardiac

minitissues, we generated a small library of scaffolds, where the simplest pore geometry, squared, but fibre spacing was varied. Uniaxial and biaxial tensile stress–strain curves are shown in figures 2(a)–(d). The 200 and 400 μm spacing scaffolds were able to extend along the *x*-direction more than 9% and 18% before undergoing permanent deformation (ε_{el}, figure 2(e)), respectively. Uniaxial mechanical tests showed that the elastic modulus decreased with an increasing fibre spacing (E_T (200 μm) = 75.48 ± 7.96 MPa; E_T (400 μm) = 55.8627 ± 7.5872 MPa, figure 2(f)). The 400 μm spacing scaffolds exhibited a lower elastic limit stress σ_{el} = 4.7337 ± 0.1656 MPa than the 200 μm one σ_{el} = 5.0315 ± 0.2040 MPa (figure 2(g)). Finally, biaxial results appeared due to the symmetric orthogonal design and pore geometry; all samples were mainly isotropic showing an isotropy ratio of. IR = 0.9717 ± 0.0614 and IR = 0.9775 ± 0.1999 for 200 and 400 μm spacing scaffolds respectively.

4.2. MEW-based cardiac minitissues are functional and show features of cardiac maturation

In order to gain specific information for the generation of the computational models, 5 × 5 mm (length/width), 200 μm spacing, square pore and ten layers mPCL scaffolds were chosen to generate human cardiac minitissues. hiPSC-CMs were embedded in GFR-MG and deposited at 1 million cells per sample on the 5 × 5 mm mats (figure 3(a)). Cells were able to quickly remodel their surrounding matrix, as evidenced by the compaction of tissues and cell elongation seen in the samples (figure 3(b)), with early, localized beats evident within the first 2 d after plating.

Figure 2. Mechanical response of the scaffolds. Under (a) uniaxial loading in *y* printing direction (b) equibiaxial loading in both *x* and *y* printing directions and corresponding deformed scaffolds (c) at 5%, 10%, 20% and 30% of uniaxial strain and (d) at 10%, 30% and 50% of equibiaxial strain (e) is the elastic limit strain ε_{el}, (f) is the tangent modulus, E_T, (g) is the elastic limit stress σ_e. **: $p < 0.01$.
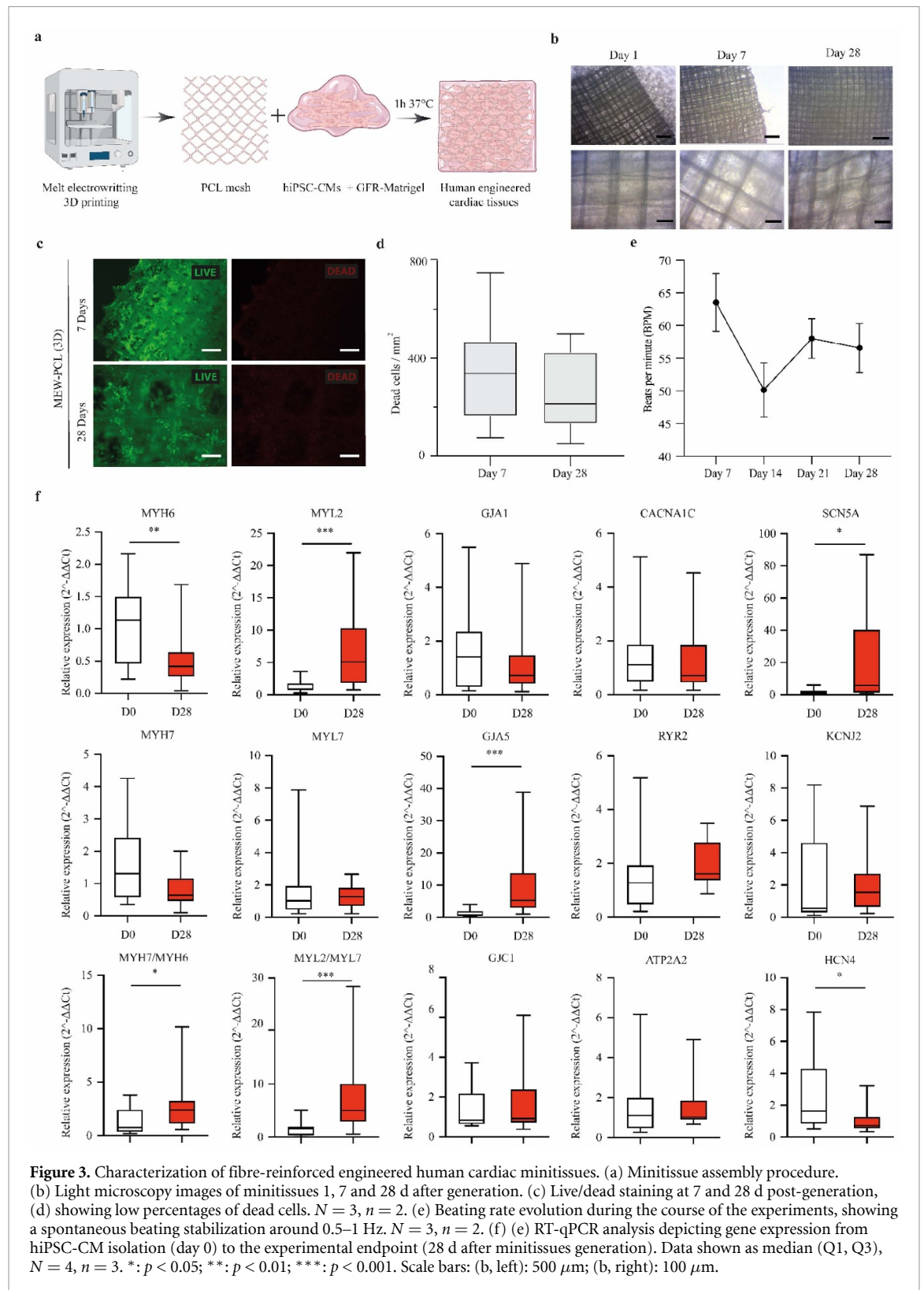
Synchronous contractions started to appear after a week in culture and were maintained for the duration of the experiments (4 weeks, movies S2 and S3 respectively). Live/dead staining (figures 3(c) and (d)) showed that most cells remained viable at both time points examined (1 and 4 weeks), with dead cells constituting a small minority, well in line with results for similar systems in cardiac tissue engineering [24, 40]. During this period and as shown in figure 3(a), tissues remained largely intact, with their beat rate becoming stabilized at 0.5–1 Hz after 1 week (figure 3(e)). Analysis of gene expression by real time quantitative polymerase chain reaction (RT-qPCR) (figure 3(f)) pointed towards a more mature phenotype by the end of the culture period, with a significant downregulation of the immature isoform of MYH6 and a significant upregulation of the ventricular isoform of myosin light chain (MYL2), which resulted in an increase in the mature/immature MYH ratio (MYH7/MYH6) and ventricular/atrial (MYL2/MYL7). Minitissues displayed an increased

expression of the fast-conducting gap junction GJA5, and of the sodium voltage-gated channel, encoded by SCN5A, pointing towards a faster conduction of the cardiac impulse and coupling, and a faster depolarization. In line with the reported stabilization of the beating rate, a significant decrease in the pacemaker signature gene HCN4, implicated in CM automaticity, was found. In summary, the selected scaffolds allow the fabrication of human cardiac minitissues, where hiPSC-CMs survive and function for up to 4 weeks, displaying a significant maturation trend at the gene expression level.
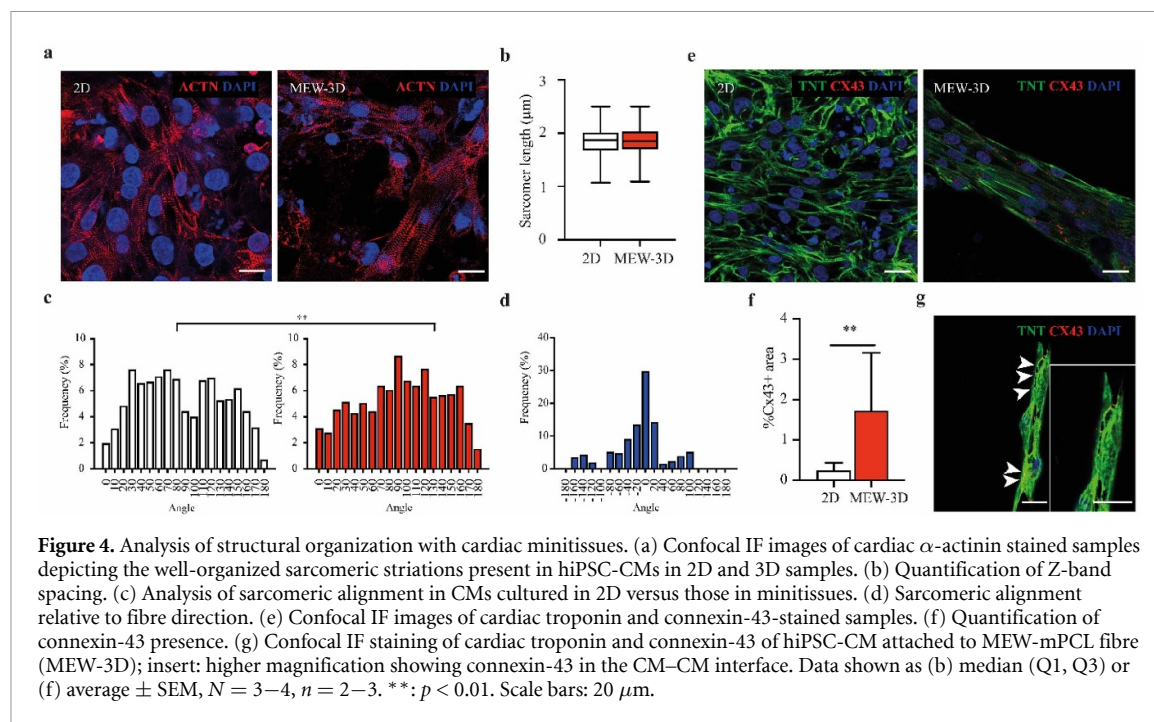
4.3. Human CMs are organized and better inter-connected in MEW-minitissues

After we had obtained basic proof of the suitability of our chosen components for building human cardiac tissues, it was crucial to determine the structural configuration of CMs within them. We employed immunofluorescent staining and confocal microscopy to obtain accurate morphometric information

Figure 3. Characterization of fibre-reinforced engineered human cardiac minitissues. (a) Minitissue assembly procedure. (b) Light microscopy images of minitissues 1, 7 and 28 d after generation. (c) Live/dead staining at 7 and 28 d post-generation, (d) showing low percentages of dead cells. $N = 3$, $n = 2$. (e) Beating rate evolution during the course of the experiments, showing a spontaneous beating stabilization around 0.5–1 Hz. $N = 3$, $n = 2$. (f) (e) RT-qPCR analysis depicting gene expression from hiPSC-CM isolation (day 0) to the experimental endpoint (28 d after minitissues generation). Data shown as median (Q1, Q3), $N = 4$, $n = 3$. *: $p < 0.05$; **: $p < 0.01$; ***: $p < 0.001$. Scale bars: (b, left): 500 μm; (b, right): 100 μm.

and compared it with conventionally cultured cells (on 2D, matrigel-coated plastic surfaces) in order to specifically gauge the magnitude of the effect. Analysis of confocal images and stacks revealed that hiPSC-CMs were randomly arranged on 2D substrates, following an isometric distribution with no directional preference. However, it was soon evident that CMs in close contact and in the vicinity of mPCL fibres

followed the printed orthogonal design (figure 4(a)). Although no difference was found in sarcomeric Z-band spacing (with 1.842 ± 0.014 μm for hiPSC-CMs on 2D surfaces and 1.87 ± 0.015 μm for those on the 3D MEW minitissues, mean $\pm$ SEM, $p = 0.469$, figure 4(b)), the alignment of sarcomeres was significantly influenced by the presence of the scaffold (figure 4(c)), with almost 60% of them arranged

Figure 4. Analysis of structural organization with cardiac minitissues. (a) Confocal IF images of cardiac α-actinin stained samples depicting the well-organized sarcomeric striations present in hiPSC-CMs in 2D and 3D samples. (b) Quantification of Z-band spacing. (c) Analysis of sarcomeric alignment in CMs cultured in 2D versus those in minitissues. (d) Sarcomeric alignment relative to fibre direction. (e) Confocal IF images of cardiac troponin and connexin-43-stained samples. (f) Quantification of connexin-43 presence. (g) Confocal IF staining of cardiac troponin and connexin-43 of hiPSC-CM attached to MEW-mPCL fibre (MEW-3D); insert: higher magnification showing connexin-43 in the CM–CM interface. Data shown as (b) median (Q1, Q3) or (f) average $\pm$ SEM, $N = 3-4$, $n = 2-3$. $**$: $p < 0.01$. Scale bars: 20 μm.

within 20° of the fibre direction (figure 4(d)). This sets out and quantifies the alignment stimulus provided by the scaffolds. However, we also noted a more prominent presence of connexin-43 (C $\times$ 43) CM–CM connections. As can be seen in figure 4(e), hiPSC-CMs on both 2D and 3D-MEW substrates presented a dotted C $\times$ 43 staining, but the presence of C $\times$ 43 was significantly higher when CMs were cultured in the 3D systems (0.246 ± 0.06 vs 1.727 ± 0.301 respectively, mean $\pm$ SEM, $p = 0.002$, figure 4(f)). As seen in figure 4(g), CMs in close contact with the mPCL fibres often had well lateralized C $\times$ 43 staining, connecting neighbouring cells. Taken together, these results point towards the capacity of the MEW scaffolds to pattern hiPSC-CMs, and to improve the electrical interconnection between them, as compared with 2D conventional culture systems.
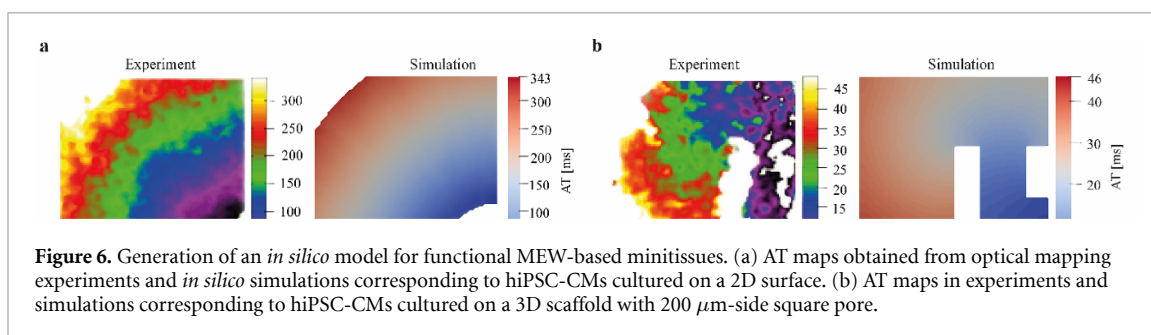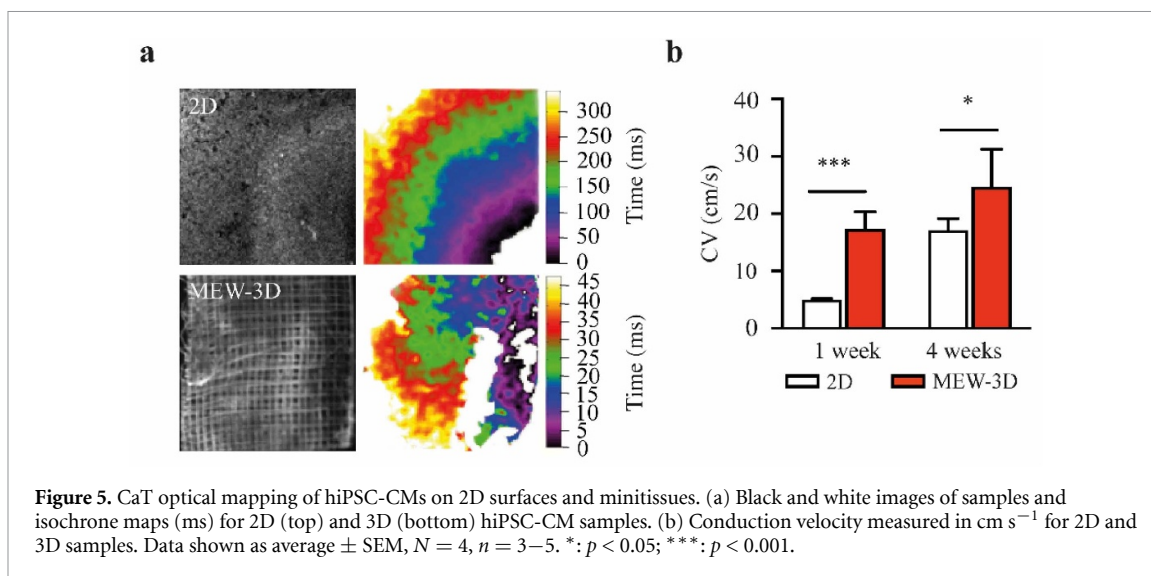
4.4. Improved cardiac function in human minitissues

Anisotropy and electrical connectivity are two features of mature cardiac tissue. As these features, also supported by the reported changes in gene expression, can affect cardiac functionality, we conducted optical mapping for CaTs both early (1 week) and late (4 weeks) after generation, in comparison with conventional 2D culture. Both 2D and the MEW-based minitissues presented a homogeneous propagation of the signal with clear foci that initiated the activation of the structures, revealing a well-connected and ordered disposition of the cells within a clear functional tissue that propagated throughout the whole surface of the samples (movie S4 and S5 for 2D and MEW respectively). Quantitative analysis of conduction velocity, exemplified on the isochronal maps

(figure 5(a)), revealed that engineered minitissues were functionally superior to hiPSC-CMs on 2D plastic surfaces, with a statistically superior conduction velocity at both 1- and 4 weeks post-fabrication (1 week: 2D: 4.985 ± 0.099 cm s^{-1}; MEW-3D: 17.297 ± 1.758 cm s^{-1}, $p < 0.001$; 4 weeks: 2D: 17.090 ± 2.017; MEW-3D: 24.653 ± 6.605, $p = 0.013$; mean $\pm$ SEM, figure 5(b)). All in all, MEW human cardiac minitissues showed a faster conduction velocity, in the range of human myocardium (10 cm s^{-1}).

4.5. *In silico* replication of cardiac function in human minitissues vs conventional hiPSC-CM cultures

The functional superiority of 3D MEW-based minitissues with respect to hiPSC-CMs cultured on 2D surfaces was further investigated *in silico*. Electrical propagation in hiPSC-CMs 2D cultures was simulated using a regular 2D mesh of isoparametric quadrilateral elements with 50 μm spacing, in which cell alignment followed a uniform statistical distribution spanning 0–180°. The tissue mesh was partitioned in several node groups, in which the funny current I_f controlling cellular automaticity was reduced by distinct factors up to 90% to reproduce the experimentally measured activation pattern. To reach the same maximum activation time (AT) as in the optical mapping experiments, the diffusion coefficient was set to 3.5×10^{-6} cm^2 ms^{-1}. A close match between simulated and experimental isochronal maps was achieved, with a maximum AT difference of 7 ms (figure 6(a)). A similar approach was followed to simulate electrical propagation in 3D MEW minitissues with square pores of 200 μm side, for which we constructed a regular 3D tissue mesh of isoparametric

Figure 5. CaT optical mapping of hiPSC-CMs on 2D surfaces and minitissues. (a) Black and white images of samples and isochrone maps (ms) for 2D (top) and 3D (bottom) hiPSC-CM samples. (b) Conduction velocity measured in cm s^{-1} for 2D and 3D samples. Data shown as average $\pm$ SEM, $N = 4$, $n = 3-5$. *: $p < 0.05$; ***: $p < 0.001$.

Figure 6. Generation of an *in silico* model for functional MEW-based minitissues. (a) AT maps obtained from optical mapping experiments and *in silico* simulations corresponding to hiPSC-CMs cultured on a 2D surface. (b) AT maps in experiments and simulations corresponding to hiPSC-CMs cultured on a 3D scaffold with 200 μm-side square pore.

hexahedral elements with 50 μm spacing. Cell alignment was set to be uniformly randomly distributed except for nodes proximal to the MEW scaffold (within 27 μm), in which it was defined to match the direction of the MEW fibres. This led to reorientation of 28.5% of the tissue nodes for the scaffold with 200 μm pore size. Inhibitions of the I_f current of up to 80% were applied in specific node groups to simulate the experimental activation pattern, with additional 20% I_{Na} reductions applied at certain node groups to represent zones devoid of cells in the experimental system. The diffusion coefficient was set to 2.72 $\times$ 10^{-4} cm^2 ms^{-1}, which allowed accurate *in silico* reproduction of the experimental isochronal map (figure 6(b)). In conclusion, our simulated isochronal maps replicated the experimentally measured maps in 2D and 3D configurations, with a relevant improvement in propagation speed induced by the use of MEW scaffolds.
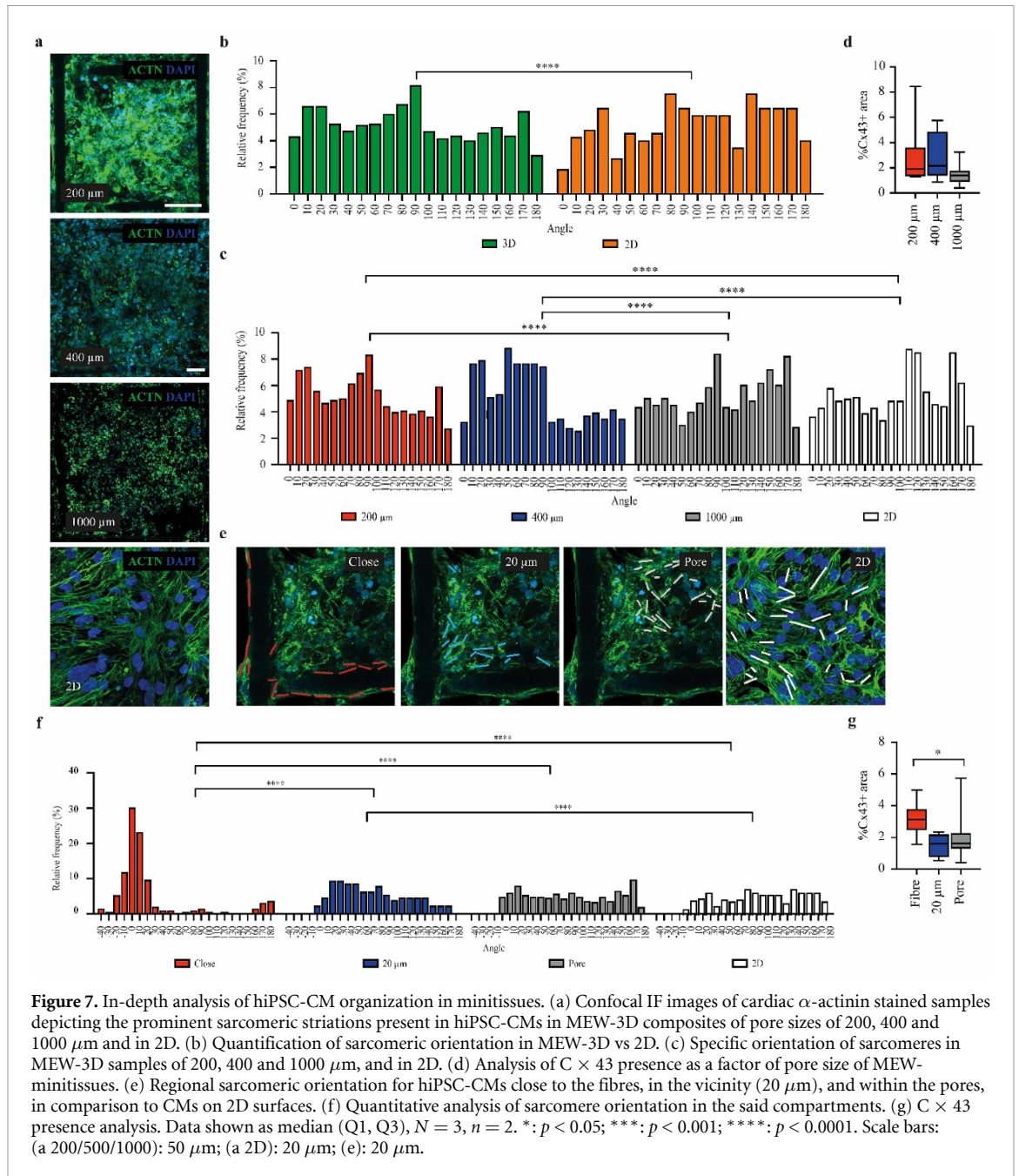
4.6. Varying pore size influences hiPSC-CM alignment without affecting CM–CM connectivity

In order to confirm the models and feed additional information into them, we printed orthogonal mPCL MEW scaffolds with different pore lengths: 200, 400 and 1000 μm. We hypothesized that the positive influence of MEW scaffolds over CM alignment would decrease with increased pore size. Therefore,

minitissues were grown for 4 weeks, stained for α-actinin and C $\times$ 43 and quantitative analysis of the confocal images and stacks was performed, for sarcomere directionality, Z-band spacing and C $\times$ 43 expression. Although no differences for Z-band spacing were found between the hiPSC-CMs populating the different scaffolds (figure S2), culture on the 3D MEW substrates was able to differentially align the cells, when all the 3D conditions were compared with those seen on 2D surfaces (figures 7(a) and (b)). Specific analysis of alignment for the different spacings showed, however, that only 200 and 400 μm scaffolds induced a statistically relevant alignment of hiPSC-CMs when compared with cells cultured on isotropic 2D plastic surfaces ($p < 0.0001$ for 200 μm vs 2D, for 200 μm vs 1000 μm, for 400 μm vs 2D and for 400 μm vs 1000 μm) (figure 7(c)). In addition, the sarcomeric orientation for CMs on both the 200 and 400 μm scaffolds was significantly more aligned than for the 1000 μm mats. No statistically significant differences were found between the different scaffolds when the presence of C $\times$ 43 was quantified (figure 7(d)).

4.7. Cell location within pore determines alignment and CM–CM connectivity

During the analysis of sarcomeric alignment, it became evident that the described effect was not homogeneous. Careful inspection of the engineered

Figure 7. In-depth analysis of hiPSC-CM organization in minitissues. (a) Confocal IF images of cardiac α-actinin stained samples depicting the prominent sarcomeric striations present in hiPSC-CMs in MEW-3D composites of pore sizes of 200, 400 and 1000 μm and in 2D. (b) Quantification of sarcomeric orientation in MEW-3D vs 2D. (c) Specific orientation of sarcomeres in MEW-3D samples of 200, 400 and 1000 μm, and in 2D. (d) Analysis of C $\times$ 43 presence as a factor of pore size of MEW-minitissues. (e) Regional sarcomeric orientation for hiPSC-CMs close to the fibres, in the vicinity (20 μm), and within the pores, in comparison to CMs on 2D surfaces. (f) Quantitative analysis of sarcomere orientation in the said compartments. (g) C $\times$ 43 presence analysis. Data shown as median (Q1, Q3), $N = 3$, $n = 2$. *: $p < 0.05$; ***: $p < 0.001$; ****: $p < 0.0001$. Scale bars: (a 200/500/1000): 50 μm; (a 2D): 20 μm; (e): 20 μm.

tissues allowed us to delimit three distinct cellular behaviours in three different areas: those cells in direct contact with the fibre, those in the immediate vicinity and those in the pore. As this differential internal organization could provide greater accuracy for the computational model, we quantified sarcomeric orientation and connectivity (% of C $\times$ 43) in three areas, specifically (a) direct contact with the mPCL fibres (termed 'Close'), (b) within 20 μm of these (termed '20 μm') and (c) in the pore (from 20 μm to the centre, termed 'Pore'), whilst we used hiPSC-CMs on 2D surfaces as control. As depicted on figures 7(e) and (f), hiPSC-CMs in the 'Close' region followed the strong alignment cues provided by the mPCL fibres, as shown by the sharp sarcomeric orientation, with over 80% of these structures following

the fibres or within 20° of them. This specific distribution was significantly different from what was found in all other three conditions. Sarcomeres in the 20 μm delimited region still were differentially aligned when compared with isometrically distributed cells (2D), though the percentage of sarcomeres within the chosen 20° of the proximal fibre orientation already dropped to less than 20%. Finally, CMs in the pore area showed no preferential alignment, with a behaviour similar to what is found on 2D surfaces (isometric distribution). When looking into CM-to-CM connection by C $\times$ 43 (figure 7(g)), cells in direct contact with the fibre had a significantly increased presence of C $\times$ 43, whilst no difference was found for those in the 20 μm or Pore regions (3.15 $\pm$ 0.406%, 1.52 $\pm$ 0.375%, 2.065 $\pm$ 0.321% for Close, 20 μm and
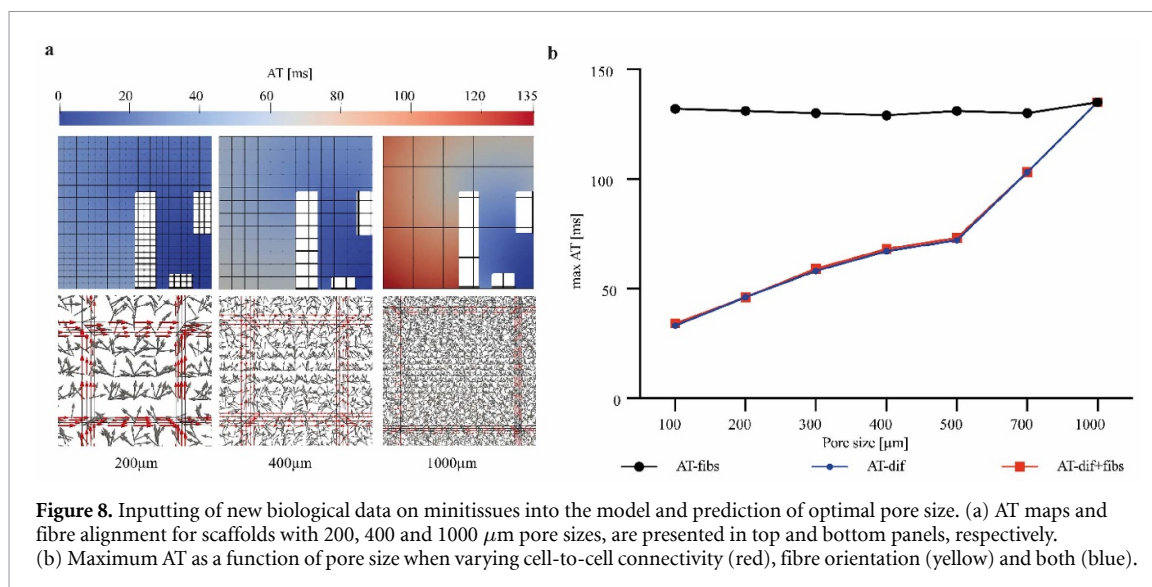
Figure 8. Inputting of new biological data on minitissues into the model and prediction of optimal pore size. (a) AT maps and fibre alignment for scaffolds with 200, 400 and 1000 μm pore sizes, are presented in top and bottom panels, respectively. (b) Maximum AT as a function of pore size when varying cell-to-cell connectivity (red), fibre orientation (yellow) and both (blue).

Pore regions respectively, $p = 0.046$ for Close vs Pore). Taken together, this highly specific regional morphometric characterization shows that alignment is lost towards the centre of the pore and with increased distance from the fibre, but that hiPSC-CMs are able to follow the predesigned fibres, and that those in direct contact with the said mPCL fibres are electrically better connected.

4.8. *In silico* identification of optimal pore size in MEW scaffolds

To further inspect the effect of the pore size on cell alignment and connectivity, we performed simulations using the tissue geometry described in section 3.5 but considering MEW scaffolds of varying pore size in the form of squares with sides ranging from 100 to 1000 μm (figure 8(a)). The proportion of tissue nodes oriented according to the scaffold's fibres remarkably decreased from the smallest to the largest pore size in concordance with a reduction in the number of nodes within 27 μm of the scaffold. In a set of simulations, we assumed a linear relationship between the degree of cell alignment in the minitissues and cell-to-cell connectivity. For the scaffold with the smallest pore size of 100 μm, 54.1% of the tissue nodes were oriented and the diffusion coefficient was set to 5.13×10^{-4} cm^2 ms^{-1}. For the largest pore size of 1000 μm, cell alignment was reduced to 4.1%, with a corresponding diffusion coefficient of 4.17×10^{-5} cm^2 ms^{-1}. To investigate which factor was mostly contributing to the increased propagation speed in 3D minitissues as compared to 2D cultures, we computed isochronal maps for each pore size under three different simulated scenarios (figure 8(b)). In the first scenario, a decrease in cell alignment with increasing pore size was simulated while the diffusion coefficient remained constant at 4.17×10^{-5} cm^2 ms^{-1} for all pore sizes. In the second scenario, random cell orientation was assigned to all

simulated meshes independent of the pore size while cell-to-cell connectivity was reduced with increasing pore size. In the third scenario, a decrease in both cell alignment and connectivity with increasing pore size was simulated. The maximum AT in the isochronal maps remained approximately constant at 131 ms for all pore sizes when cell-to-cell connectivity was not varied. When including variations in cell-to-cell connectivity proportional to variations in cell alignment, the maximal AT was remarkably reduced from 135 ms for a pore size of 1000 μm to 34 ms for a pore size of 100 μm. These findings demonstrate that cell-to-cell connectivity plays a highly relevant role in the activation of scaffolds, with smaller pore sizes leading to faster activation. This serves to highlight the role of increased C $\times$ 43 expression in the electrical activity of cells cultured in MEW scaffolds, particularly for small-to-medium scaffold pore sizes, as in the experimental evidence reported above. Moreover, our simulations generate evidence that an optimal pore size would be as small as 100 μm.

5. Discussion

The aim of the present study was to develop new tools based on computational modelling that enable an *in silico* prediction of changes occurring in the period after cardiac engineered tissue fabrication. To this end, we firstly examined the functional and structural characteristics of fibre-reinforced human engineered-cardiac tissues built using MEW, in order to input this information to computational simulations. Our results show that human cardiac cells (hiPSC-CMs) form viable and contractile minitissues whose functionality can be stably maintained for at least 4 weeks. These tissues matured over time, as shown by their gene expression and the increase in CV, reaching levels on the same order of magnitude as the natural human myocardium (10 cm s^{-1}). A more specific

structural examination determined that the cells followed an overall alignment dictated by the MEW PCL fibres and had an increased presence of the fast connexin C × 43, pointing towards a better electrical interconnection. The former effect on cellular alignment was mostly evident in the proximity of the polymeric fibres, as it disappeared when pore size in the MEW structure was enlarged, although the increase in C × 43 was maintained. The cells in close contact with the fibres displayed an even higher presence of C × 43 when compared with those located over 20 μm from them. All this specific information was fed into an *in silico* model, that was able to predict the relationship between pore size and the resulting minitissue functionality.

Cardiac tissue engineering has traditionally sought to faithfully replicate the natural human myocardium, including its cellular and extracellular components, as well as its physical properties. In order to achieve this, ECM-mimics in the form of hydrogels, either natural such as collagen type I [41] or fibrin [42], or synthetic such as GelMA [43] or PVA [44] have been extensively explored. However, though these hydrogels adequately mimic the tissue's Young's modulus (in the range of 10 s of kPa), their tensile strength, crucial to sustain the constant cycles of filling-pumping, is significantly inferior. Composites formed by supplementing mechanical reinforcers such as nanoparticles, reversible crosslinks or fibres [45–47], have contributed to strategies that enhance the mechanical properties of the resulting tissue. In this area, MEW stands out for it superior capacity to support this strategy. First, it demands very little volume [21], unlike other widespread melt-based additive manufacturing technologies like fused deposition modelling, where fibres are orders of magnitude larger. This also allows cells to interact with features of a similar size to themselves. Secondly, unlike solution electrospinning, the capacity of MEW to control fibre deposition make it possible to tailor the desired mechanical properties to those of the tissue to be produced [24, 40, 71, 72]. In our research, we designed the simplest isometric (square pore) scaffolds in order to be able to relate the biological results to the obtained mechanics and structure in a straightforward way. We chose Matrigel as the ECM mimic here, in spite of its drawbacks (mainly, its undefined nature and lot-to-lot variability) because of its high biocompatibility and transient nature, which enable the hiPSC-CMs to connect early on after minitissue formation and to interact unhindered with the MEW-PCL fibres. Despite several reports highlighting the importance of the presence of stromal cells, either fibroblasts or mesenquimal cells, for the formation of cardiac tissues *in vitro* [11, 50, 51], this was not the case in our study. Although it is plausible, as suggested by others [24], that the presence of fibres may be enough to ensure the formation of the tissues, it is possible that in our case, non-CMs in the

cellular preparation (up to a maximum of 10%) could contribute to this stromal fraction.

Our biological analysis of the human cardiac minitissues revealed several features of an ongoing maturation process, mainly highlighted by the increase in CV for the MEW-3D minitissues over that of conventionally cultured hiPSC-CMs (2D). Although 2D-maintained cells improved their functionality over the 4 week period, hiPSC-CMs in the 3D environment propagated the calcium waves significantly faster. This is also supported by the increase in expression of SCN5A over time, which could point towards a faster depolarization during phase 0 of the AP [52], and of GJA5 (encoding the fast connexin C × 40), added to the increased presence of C × 43 in the 3D tissues in comparison with the 2D cultures. Both C × 40 and C × 43 are fast conducting gap junctions allowing the passing of ions and the coordinated propagation of the cardiac AP between connected cells, indirectly supporting the observed functional outcome. Added to this, human MEW-based cardiac minitissues demonstrated a decreasing expression of the immature isoform of MYH6 (encoding for the alpha-isoform of the protein), and increased the ventricular form of the MYL2, which led to an increase in the MYH7/MYH6 (mature/immature) and MYL2/MYL7 (ventricular/atrial) ratios respectively, both of which are related to improved maturation, as reported for other engineered systems such as in the work by Ronaldson-Bouchard *et al* with collagen type-I based tissues, Ronaldson-Bouchard *et al* with fibrin-based constructs subjected to electrical stimulus or Kit-Anan *et al* using PDMS microwells [14, 41, 53], probably pointing more to the effect of the 3D environment rather than to a material-specific response. A note of caution must be raised regarding this maturation, as, in spite of the mentioned findings, the cells in our minitissues still fall short of the characteristics found in adult human CMs. These include structural features such as presence of T-tubuli, higher mitochondria content, longer sarcomeres (close to 2.2 μm for Z-band spacing at relaxation), highly patterned C × 43 or larger size, as well as functional differences as still higher CV (reviewed in [48]).

We used the optical mapping information to develop the first computational simulations able to accurately reproduce the experimental results and make predictions on the electrical behaviour of minitissues. To generate *in silico* models that can help in building advanced human cardiac tissues and predicting their evolution after fabrication, we thought it crucial to understand how cells were organized within the engineered systems after the 4 week culture period. Human iPSC-CMs arranged themselves in a specific fashion when included in the 3D MEW composite tissues. Cells were able to follow the pattern of the PCL fibres, similarly to what has been described for PDMS features [49, 53], electrospun matrices

[54], or carbon nanotube-doped substrates [55]. By varying the pore size of the scaffolds, we demonstrated that the overall alignment effect was lost when the pores were sufficiently large (1000 μm), where cellular distribution of alignment behaved more similarly to the isotropic arrangement found on 2D surfaces, and where no preferential direction or cue is provided. We gauged the magnitude of this effect and its specific location within the tissue structure. As expected, the strongest alignment effect could be found when CMs directly interacted with the MEW fibres, and it was preserved within the neighbouring cellular layers (approximately up to 20–30 μm away). In contrast, cells beyond that limit (within the pore, not directly exposed to the alignment cues) were randomly arranged and behaved more similarly to cells cultured in 2D. In consequence, the larger the pore, the smaller the alignment stimulus and effect, as the amount of fibre decreases with increased pore size. Given the importance of aligned CM contraction for the generation of relevant pumping forces, the capacity to precisely control this feature is fundamental for the efficient mimicry of the fabricated construct. Surprisingly, although hiPSC-CMs showed a higher presence of C $\times$ 43 when included in the 3D environment of the MEW composites in comparison to cells in 2D, those cells in direct contact with the fibres had even higher levels when compared to the other two locations. This latter piece of information potentially has important implications as these cells could act as 'conduction highways' and impact the overall engineered tissue performance by tuning the transmission of the cardiac impulse. This can be crucial for building better and more biomimetic engineered cardiac tissues. Novel MEW-scaffold designs could be produced in which, by changing the printing path whilst complying with the desired macroscopic (at tissue level) mechanical properties, an increased alignment stimulus could be provided by decreasing the pore size and increasing the number of fibres oriented in a single direction, thus better replicating the myocardial anisotropy. In line with our results, this would be anticipated to increase conduction speed in the chosen direction. Also, pore geometry could be tuned to increase flexibility and contraction capacity, as already shown for hexagons and sinusoidal patters [24, 48].

Design is inherent to additive manufacturing. Traditionally, this has come from medical imaging data such as MRI or CT scans. The information is segmented and transformed into printable files that will enable the selected technology to reproduce the natural architecture. However, this workflow is imperfect, as it does not always take into account the specifics of tissue maturation after assembly. In consequence, even the most accurately manufactured and bioinspired engineered tissue could fail to deliver the expected functionality if during the evolution after fabrication, its constituents are rearranged in the

wrong fashion. Our work takes the first steps towards developing *in silico* tools able to perform a design-to-evolution prediction. These will, in the near future, allow us to fine-tune the fabrication and assembly procedures for a final engineered tissue displaying the required structural and functional characteristics. We used the simplest design and components (square isometric pores, transient hydrogel, uniphenotypical cellular composition) to deliver this first generation simulation. The model is already able to adequatedly simulate the relationship between pore size and resulting biological performance (AT). Our next steps will be directed towards increasing its complexity by obtaining novel information in different areas. These include (a) varying the pore geometry, orientation and number of layers to accommodate complex structures such as those already reported, including hexagons and auxetic structures [24, 56], (b) analyse the effect of the structure on the overall mechanical properties of the scaffold, (c) including the specific material properties, as well as novel features such as conductivity [56–58], (d) increasing the complexity of the cellular components to make it more representative of the native cardiac tissue, by introducing fibroblasts, vascular and pacemaker cells, all of which are now attainable through specific differentiation of hiPSCs [6, 59, 60], (e) enhanced functionality through maturation via the implementation of electromechanical, hormonal or metabolic stimulation [14, 61, 62], and (f) increased biological information through the use of novel genomics procedures and analysis, including single cell sequencing [63].

It is important to note that, in spite of the tensile properties of the MEW-mPCL scaffolds, well above the range reported for human myocardium, our minitissues are functional and show macroscopic beating. This probably results from their overall mechanical properties (including the hydrogel and cellular components) providing a suitable environment for hiPSC-CM to contract the whole structure. Subsequent work will investigate this in depth. This underlines the importance of having an optimal understanding of the mismatch between the mechanical properties of the individual components in a given engineered tissue, versus the properties of that tissue as a whole. Although mPCL is the gold standard material for MEW, other polymers with more suitable mechanical properties, such as highly elastic poly(L-lactide-co-ε-caprolactone) [64], would be highly beneficial for their use in the cardiac field. In addition, the long degradation time of mPCL (in the range of years) [65] can also be detrimental for the application.

Building biomimetic, functional and mature human myocardium has significant application venues. Firstly, as tissue models, they could allow the investigation of human cardiac physiology and pathology. Added to the potential of deriving hiPSCs from patients or to simulate disease conditions *in vitro*,

they could help fill in knowledge gaps currently unaddresseable due to the scarcity of human primary heart tissue [66]. Although hiPSC-derived cells in 2D or as organoids are undergoing intense research in this area [67, 68], lack of adequate maturity or 3D organization are some of the main roadblocks that the present approach could help lift. Secondly, as drug testing platforms. Albeit the need for cell numbers in the range of millions precludes their use in high throughput testing, mature electrical properties can position MEW-based minitissues as a safer and more reliable testing system for compound arrhythmogenicity, currently one of the main causes of drug withdrawal [69]. Lastly, this technology has a superb potential for the building of human myocardium for therapeutic purposes. MEW scaffolds can be printed to a relevant thickness with fine control of fibre deposition [23], enabling the recapitulation of the specific cellular alignment within the myocardial wall, which added to the recent development of methodologies to increase the yield of CMs from hiPSC differentiation procedures [70] makes this aim more feasible than ever.

In summary, we fabricated human cardiac engineered tissues employing hiPSC-CMs and an ECM mimic based on a fast-degrading hydrogel (Matrigel), reinforced with a 3D-MEW fibrous structure. These minitissues present contractile activity, and show maturation over time in terms of gene expression and functionality. In addition, the presence of the 3D MEW reinforcement is able to deliver a specific hiPSC-CM alignment and a higher interconnectivity through a stronger presence of C × 43. By inputting the collected biological information into novel computational simulations, our work outlines the path towards the development of advanced tools that will allow the *in silico* design of new constructs with enhanced and accurately predicted functional capacity. This strategy can easily be applied to most additive manufacturing technologies that allow for a controlled deposition of material or cells.

Data availability statement

The data that support the findings of this study are available upon reasonable request from the authors.

Acknowledgments

Funding

Conflict of interest

Authors declare none.

ORCID iDs

Elena M de-Juan-Pardo ● https://orcid.org/0000-0001-9005-7497
Felipe Atienza ● https://orcid.org/0000-0002-9596-7649
María Eugenia Fernández-Santos ●
https://orcid.org/0000-0001-9229-0022
Manuel Doblaré ● https://orcid.org/0000-0001-8741-6452
Francisco Fernández-Avilés ●
https://orcid.org/0000-0001-5501-5275
Manuel M Mazo ● https://orcid.org/0000-0002-6250-5579

References

[1] Roth G A *et al* 2020 Global burden of cardiovascular diseases and risk factors, 1990-2019: update from the GBD 2019 study *J. Am. Coll. Cardiol.* **76** 2982–3021

[2] Figtree G A *et al* 2021 A call to action for new global approaches to cardiovascular disease drug solutions *Eur. Heart J.* **42** 1464–75

[3] Montero P, Flandes-Iparraguirre M, Musquiz S, Pérez Araluce M, Plano D, Sanmartín C, Orive G, Gavira J J, Prosper F and Mazo M M 2020 Cells, materials, and fabrication processes for cardiac tissue engineering *Front. Bioeng. Biotechnol.* **8** 955

[4] Burridge P W *et al* 2014 Chemically defined generation of human cardiomyocytes *Nat. Methods* **11** 855–60

[5] Williams I M and Wu J C 2019 Generation of endothelial cells from human pluripotent stem cells *Arterioscler. Thromb. Vasc. Biol.* **39** 1317–29

[6] Zhang H, Tian L, Shen M, Wu H, Gu M, Tu C, Paik D T and Wu J C 2019 Generation of quiescent cardiac fibroblasts from human induced pluripotent stem cells for *in vitro* modeling of cardiac fibrosis *Circ. Res.* **125** 552–66

[7] Macqueen L A *et al* 2018 A tissue-engineered scale model of the heart ventricle *Nat. Biomed. Eng.* **2** 930–41

[8] Noor N, Shapira A, Edri R, Gal I, Wertheim L and Dvir T 2019 3D printing of personalized thick and perfusable cardiac patches and hearts *Adv. Sci.* **6** 1900344

[9] Daly A C, Davidson M D and Burdick J A 2021 3D bioprinting of high cell-density heterogeneous tissue models through spheroid fusion within self-healing hydrogels *Nat. Commun.* **12** 1–13

[10] Daly A C, Prendergast M E, Hughes A J and Burdick J A 2021 Bioprinting for the biologist *Cell* **184** 18–32

[11] Giacomelli E *et al* 2020 Human-iPSC-derived cardiac stromal cells enhance maturation in 3D cardiac microtissues and reveal non-cardiomyocyte contributions to heart disease *Cell Stem Cell* **26** 862–79

[12] Dias T P, Pinto S N, Santos J I, Fernandes T G, Fernandes F, Diogo M M, Prieto M and Cabral J M S 2018 Biophysical study of human induced pluripotent stem cell-derived cardiomyocyte structural maturation during long-term culture *Biochem. Biophys. Res. Commun.* **499** 611–7

[13] Godier-Furnémont A F G, Tiburcy M, Wagner E, Dewenter M, Lämmle S, El-Armouche A, Lehnart S E, Vunjak-Novakovic G and Zimmermann W H 2015 Physiologic force-frequency response in engineered heart muscle by electromechanical stimulation *Biomaterials* **60** 82–91

[14] Ronaldson-Bouchard K, Ma S P, Yeager K, Chen T, Song L J, Sirabella D, Morikawa K, Teles D, Yazawa M and Vunjak-Novakovic G 2018 Advanced maturation of human cardiac tissue grown from pluripotent stem cells *Nature* **556** 239–43

[15] Chong J J H *et al* 2014 Human embryonic-stem-cell-derived cardiomyocytes regenerate non-human primate hearts *Nature* **510** 273–7

[16] Ye L *et al* 2015 Cardiac repair in a porcine model of acute myocardial infarction with human induced pluripotent stem cell-derived cardiovascular cells *Cell Stem Cell* **16** 102

[17] Shiba Y *et al* 2016 Allogeneic transplantation of iPS cell-derived cardiomyocytes regenerates primate hearts *Nature* **538** 388–91

[18] Fisch P, Holub M and Zenobi-Wong M 2021 Improved accuracy and precision of bioprinting through progressive cavity pump-controlled extrusion *Biofabrication* **13** 015012

[19] Hrynevich A, Liashenko I, Dalton P D, Hrynevich A, Liashenko I and Dalton P D 2020 Accurate prediction of melt electrowritten laydown patterns from simple geometrical considerations *Adv. Mater. Technol.* **5** 2000772

[20] Edri R *et al* 2019 Personalized hydrogels for engineering diverse fully autologous tissue implants *Adv. Mater.* **31** 1–9

[21] Bas O, de-Juan-Pardo E M, Chhaya M P, Wunner F M, Jeon J E, Klein T J and Hutmacher D W 2015 Enhancing structural integrity of hydrogels by using highly organised melt electrospun fibre constructs *Eur. Polym. J.* **72** 451–63

[22] Brown T D, Dalton P D and Hutmacher D W 2011 Direct writing by way of melt electrospinning *Adv. Mater.* **23** 5651–7

[23] Wunner F M, Wille M L, Noonan T G, Bas O, Dalton P D, De-Juan-Pardo E M and Hutmacher D W 2018 Melt electrospinning writing of highly ordered large volume scaffold architectures *Adv. Mater.* **30** 1–6

[24] Castilho M, van Mil A, Maher M, Metz C H G, Hochleitner G, Groll J, Doevendans P A, Ito K, Sluijter J P G and Malda J 2018 Melt electrowriting allows tailored microstructural and mechanical design of scaffolds to advance functional human myocardial tissue formation *Adv. Funct. Mater.* **28** 1803151

[25] Gao L *et al* 2017 Myocardial tissue engineering with cells derived from human-induced pluripotent stem cells and a native-like, high-resolution, 3-dimensionally printed scaffold *Circ. Res.* **120** 1318–25

[26] Stuckensen K *et al* 2019 Anisotropic cryostructured collagen scaffolds for efficient delivery of RhBMP-2 and enhanced bone regeneration *Materials* **12** 3105

[27] Valls-Margarit M *et al* 2019 Engineered macroscale cardiac constructs elicit human myocardial tissue-like functionality *Stem Cell Rep.* **13** 207–20

[28] Araña M, Peña E, Abizanda G, Cilla M, Ochoa I, Gavira J J, Espinosa G, Doblaré M, Pelacho B and Prosper F 2013 Preparation and characterization of collagen-based ADSC-carrier sheets for cardiovascular application *Acta Biomater.* **9** 6075–83

[29] Lee P, Bollensdorff C, Quinn T A, Wuskell J P, Loew L M and Kohl P 2011 Single-sensor system for spatially resolved, continuous, and multiparametric optical mapping of cardiac tissue *Hear Rhythm* **8** 1482–91

[30] Gómez-Cid L, Moro-López M, De La Nava A S, Hernández-Romero I, Fernández A I, Suárez-Sancho S, Atienza F, Grigorian-Shamagian L and Fernández-Avilés F 2020 Electrophysiological effects of extracellular vesicles secreted by cardiosphere-derived cells: unraveling the antiarrhythmic properties of cell therapies *Processes* **8** 924

[31] Del-Canto I, Gómez-Cid L, Hernández-Romero I, Guillem M S, Fernández-Santos M E, Atienza F, Such L, Fernández-Avilés F, Chorro F J and Climent A M 2020 Ranolazine-mediated attenuation of mechanoelectric feedback in atrial myocyte monolayers *Front. Physiol.* **11** 922

[32] Laughner J I, Ng F S, Sulkin M S, Martin Arthur R and Efimov I R 2012 Processing and analysis of cardiac optical mapping data obtained with potentiometric dyes *Am. J. Physiol. Heart Circ. Physiol.* **303** 753–65

[33] Paci M, Hyttinen J, Aalto-Setälä K and Severi S 2013 Computational models of ventricular- and atrial-like human induced pluripotent stem cell derived cardiomyocytes *Ann. Biomed. Eng.* **41** 2334–48

[34] Mountris K A and Pueyo E 2020 The radial point interpolation mixed collocation method for the solution of transient diffusion problems *Eng. Anal. Bound. Elem.* **121** 207–16

[35] Mountris K A and Pueyo E 2021 Cardiac electrophysiology meshfree modeling through the mixed collocation method 2110.06671

[36] Mountris K A and Pueyo E 2021 A dual adaptive explicit time integration algorithm for efficiently solving the cardiac monodomain equation *Int. J. Numer. Methods Biomed. Eng.* **37** e3461

[37] Kade J C and Dalton P D 2021 Polymers for melt electrowriting *Adv. Healthcare Mater.* **10** 2001232

[38] Jacot J G, McCulloch A D and Omens J H 2008 Substrate stiffness affects the functional maturation of neonatal rat ventricular myocytes *Biophys. J.* **95** 3479–87

[39] Pandey P *et al* 2018 Cardiomyocytes sense matrix rigidity through a combination of muscle and non-muscle myosin contractions *Dev. Cell* **44** 326–36

[40] Castilho M, Feyen D, Flandes-Iparraguirre M, Hochleitner G, Groll J, Doevendans P A F, Vermonden T, Ito K, Sluijter J P G and Malda J 2017 Melt electrospinning writing of poly-hydroxymethylglycolide-co-ε-caprolactone-based scaffolds for cardiac tissue engineering *Adv. Healthcare Mater.* **6** 1700311

[41] Tiburcy M *et al* 2017 Defined engineered human myocardium with advanced maturation for applications in heart failure modeling and repair *Circulation* **135** 1832–47

[42] Jabbour R J *et al* 2021 *In vivo* grafting of large engineered heart tissue patches for cardiac repair *JCI Insight* **6** e144068

[43] Annabi N *et al* 2016 Highly elastic and conductive human-based protein hybrid hydrogels *Adv. Mater.* **28** 40–49

[44] Wu F, Gao A, Liu J, Shen Y, Xu P, Meng J, Wen T, Xu L and Xu H 2018 High modulus conductive hydrogels enhance *in vitro* maturation and contractile function of primary cardiomyocytes for uses in drug screening *Adv. Healthcare Mater.* **7** 1800990

[45] Zhu K *et al* 2017 Gold nanocomposite bioink for printing 3D cardiac constructs *Adv. Funct. Mater.* **27** 1–12

[46] Akentjew T L *et al* 2019 Author Correction: rapid fabrication of reinforced and cell-laden vascular grafts structurally inspired by human coronary arteries *Nat. Commun.* **10** 1–15

[47] Lorson T, Jaksch S, Lü M M, Jü T, Rgen Groll J, Lü T and Luxenhofer R 2017 A thermogelling supramolecular hydrogel with sponge-like morphology as a cytocompatible bioink *Biomacromolecules* **18** 2161–71

[48] Karbassi E, Fenix A, Marchiano S, Muraoka N, Nakamura K, Yang X and Murry C E 2020 Cardiomyocyte maturation: advances in knowledge and implications for regenerative medicine *Nat. Rev. Cardiol.* **17** 341–59

[49] Abadi P P S S *et al* 2018 Engineering of mature human induced pluripotent stem cell-derived cardiomyocytes using substrates with multiscale topography *Adv. Funct. Mater.* **28** 1–11

[50] Iseoka H *et al* 2018 Pivotal role of non-cardiomyocytes in electromechanical and therapeutic potential of induced pluripotent stem cell-derived engineered cardiac tissue *Tissue Eng.* A **2016** 0535

[51] Hookway T A, Matthys O B, Mendoza-Camacho F N, Rains S, Sepulveda J E, Joy D A and Mcdevitt T C 2019 Phenotypic variation between stromal cells differentially impacts engineered cardiac tissue function *Tissue Eng.* A **25** 773–85

[52] Veerman C C *et al* 2017 Switch from fetal to adult SCN5A isoform in human induced pluripotent stem cell—derived cardiomyocytes unmasks the cellular phenotype of a conduction disease—causing mutation *J. Am. Heart Assoc.* **6** e005135

[53] Kit-Anan W *et al* 2021 Multiplexing physical stimulation on single human induced pluripotent stem cell-derived cardiomyocytes for phenotype modulation *Biofabrication* **13** 025004

[54] Fleischer S, Shapira A, Regev O, Nseir N, Zussman E and Dvir T 2014 Albumin fiber scaffolds for engineering functional cardiac tissues *Biotechnol. Bioeng.* **111** 1246–57

[55] Roshanbinfar K, Mohammadi Z, Sheikh-Mahdi Mesgar A, Dehghan M M, Oommen O P, Hilborn J and Engel F B 2019 Carbon nanotube doped pericardial matrix derived electroconductive biohybrid hydrogel for cardiac tissue engineering *Biomater. Sci.* **7** 3906–17

[56] Olvera D, Sohrabi Molina M, Hendy G and Monaghan M G 2020 Electroconductive melt electrowritten patches matching the mechanical anisotropy of human myocardium *Adv. Funct. Mater.* **30** 1–10

[57] Kapnisi M *et al* 2018 Auxetic cardiac patches with tunable mechanical and conductive properties toward treating myocardial infarction *Adv. Funct. Mater.* **28** 1800618

[58] Mawad D *et al* 2016 A conducting polymer with enhanced electronic stability applied in cardiac models *Sci. Adv.* **2** e1601007

[59] Patsch C *et al* 2015 Generation of vascular endothelial and smooth muscle cells from human pluripotent stem cells *Sci. Cell Biol.* **17** 994–1003

[60] Protze S I, Liu J, Nussinovitch U, Ohana L, Backx P H, Gepstein L and Keller G M 2016 Sinoatrial node cardiomyocytes derived from human pluripotent cells function as a biological pacemaker *Nat. Biotechnol.* **35** 56–68

[61] Parikh S S *et al* 2017 Thyroid and glucocorticoid hormones promote functional T-tubule development in human-induced pluripotent stem cell-derived cardiomyocytes *Circ. Res.* **121** 1323–30

[62] Gomes-Alves P *et al* 2016 *In vitro* expansion of human cardiac progenitor cells: exploring 'omics tools for characterization of cell-based allogeneic products *Transl. Res.* **171** 96–110.e3

[63] Ruiz-Villalba A *et al* 2020 Single-cell RNA sequencing analysis reveals a crucial role for CTHRC1 (collagen triple helix repeat containing 1) cardiac fibroblasts after myocardial infarction *Circulation* **142** 1831–47

[64] Sanchez Diaz R, Park J-R, Rodrigues L L, Dalton P D, De-Juan-Pardo E M and Dargaville T R 2022 Highly elastic scaffolds produced by melt electrowriting of poly(L-lactide-co-ε-caprolactone) *Adv. Mater. Technol.* **7** 2100508

[65] Woodruff M A and Hutmacher D W 2010 The return of a forgotten polymer—polycaprolactone in the 21st century *Prog. Polym. Sci.* **35** 1217–56

[66] Watson S A *et al* 2019 Biomimetic electromechanical stimulation to maintain adult myocardial slices *in vitro Nat. Commun.* **10** 2168

[67] Richards D J *et al* 2020 Human cardiac organoids for the modelling of myocardial infarction and drug cardiotoxicity *Nat. Biomed. Eng.* **4** 446–62

[68] Wu H *et al* 2019 Modelling diastolic dysfunction in induced pluripotent stem cell-derived cardiomyocytes from hypertrophic cardiomyopathy patients *Eur. Heart J.* **40** 3685–95

[69] Laverty H G *et al* 2011 How can we improve our understanding of cardiovascular safety liabilities to develop safer medicines? *Br. J. Pharmacol.* **163** 675–93

[70] Buikema J W *et al* 2020 Wnt activation and reduced cell-cell contact synergistically induce massive expansion of functional human iPSC-derived cardiomyocytes *Cell Stem Cell* **27** 50–63.e5

[71] Saidy N T, Wolf F, Bas O, Keijdener H, Hutmacher D W, Mela P and De-Juan-Pardo E M 2019 Biologically inspired scaffolds for heart valve tissue engineering via melt electrowriting *Small* **15** e1900873

[72] Saidy N T *et al* 2022 Spatially heterogeneous tubular scaffolds for *in situ* heart valve tissue engineering using melt electrowriting *Adv. Funct. Mater.* **32** 2110716